**REGULAR PAPER**

# Investigation of Machining Stability Considering Thermal and Rotation Effect: Effectiveness of Impact Excitation for a Rotating Spindle

Minsu Kim[1] · Hyung-Wook Park[2] · Sun-Kyu Lee[1]

## Abstract

This study investigates machining stability considering the rotational and thermal effects of a spindle-bearing system. Conventional method for analysis of machining stability only has regarded the static response of spindle system, which does not represent actual machining conditions as some investigations mentioned. Bearing stiffness change caused by a contact angle change is applied to the analytical approach for a dynamics of spindle system. At the same time, in a frequency response function (FRF) of rotating spindle, disturbance-induced signals are included such as a slip between hammer and tool, a spindle run-out and a noise due to insufficient impulse force. In this paper, a conventional impact exciting method which has been popular for characterization is refined in order to obtain dynamic characteristics of rotating spindle-bearing system on the consideration of coherence function. Those disturbances in the output signal are remarkably reduced through finding both the optimal conditions in terms of impulse force and the filtering of false responses. The proposed refined impact exciting tests, which can manage both rotational and thermal effects under rotating conditions, lead to provide FRFs matching more accurately. Stability lobe diagrams (SLDs) derived from FRFs obtained by experiments were derived to evaluate the effectiveness of the dynamic characteristic change in bearing-spindle systems. As a result, the axial depth of cut limitations at chatter occurrence points were well matched to actual depth limits with a deviation of 3% or less. Chatter vibration generation conditions can be well estimated, which proved that SLDs considering the dynamic characteristic of spindle-bearing system reveal the actual cutting condition since it includes thermal and rotation effects of spindle-bearing system during milling process.

**Keywords** Stability lobe diagram (SLD) · End milling · Thermal effect · Rotational effect · Spindle-bearing system

## List of Symbols

| | |
|---|---|
| Q | Normal force on rolling element (N) |
| K | Load–deflection factor or cutting force coefficient (N/mm$^2$) |
| δ | Deformation (mm) |
| F | Force (N) |
| $F_c$ | Centrifugal force (N) |
| α | Contact angle (°) |
| ε | Thermal expansion (mm) |
| $M_v$ | Viscous friction torque (N mm) |
| $d_m$ | Pitch diameter of bearing (mm) |
| f | Raceway's groove radius/ball diameter |
| $v_{vis}$ | Kinematic viscosity of bearing lubrication (mm$^2$/s) |
| S | Rotational speed of spindle (RPM) |
| ν | Poisson's ratio |
| r | Radius (mm) |
| T | Temperature (K) |
| f | Raceway's groove radius/ball diameter |
| B | Total curvature (mm) |
| D | Ball diameter (mm) |
| E | Young's modulus (N/mm$^2$) |
| A, B | Coefficients of second-order equation |
| $M_{gj}$ | Gyroscopic moment (N mm) |
| λ | Gyroscopic moment coefficient |
| h | Dynamic chip thickness (mm) |
| $s_t$ | Static, uncut chip thickness (mm) |
| φ | Auxiliary angle or tooth angle position (°) |

✉ Sun-Kyu Lee
skyee@gist.ac.kr

Minsu Kim
minsukim0901@gmail.com

Hyung-Wook Park
hwpark@unist.ac.kr

1   School of Mechanical Engineering, Gwangju Institute of Science and Technology, 123, Cheomdangwagi-ro, Buk-gu, Gwangju 61005, South Korea

2   School of Mechanical and Aeronautical Engineering, Ulsan National Institute of Science and Technology, 50 UNIST-Gil, Ulsan 44919, South Korea

| | |
|---|---|
| $a_d$ | Axial depth of cut (mm) |
| $\alpha$ | Directional milling force coefficient |
| N | Number of cutters |
| $\eta$ | Phase distance in one tooth period (°/tooth) |
| $\Phi$ | Frequency response function |
| $\omega_c$ | Chatter frequency (Hz) |
| $\Lambda$ | Eigenvalue |
| $\epsilon$ | Phase shift between the inner and outer modulations (°) |

**Subscripts**

| | |
|---|---|
| $a$ | Axial direction |
| $r$ | Radial direction |
| $i$ | Inner race or contact |
| $o$ | Outer race or contact |
| $h$ | Bearing housing |
| s | Shaft |
| $t$ | Tangential direction |
| $th$ | Thermally induced component |
| $rot$ | Rotational |
| $j$ | Position of rolling element inside bearing or $j^{th}$ cutter of end mill |
| xx, xy, yx, yy | Direction of frequency response function in cutting force matrix |
| $st, ex$ | Start and exit angle |
| $R$ | Real part |
| $I$ | Imaginary part |

## 1 Introduction

Many engineers and researchers have investigated the chatter phenomenon that occurs during turning, drilling, and milling operations conducted with computer numerically controlled (CNC) machine tools. Basically, this work assumes that a cutting tool and workpiece mounted on the machine tool have mutually influenced cutting forces or vibrations that are exerted on each other. Even though all effective conditions are carefully considered, forced and self-excited vibrations during the cutting process are difficult to avoid [1, 2]. Previous investigations have been focused on simple features induced by cutting conditions, such as a radial immersion [3] or a type of relative motion between the workpiece and tool [4]. In general, a chatter vibration is mainly affected by characteristics of the machine tools, which can be first realized in spindle-holder-tool assemblies or the frequency response reflection in the time domain [5, 6]. To examine the dynamic characteristic changes of high-speed spindle systems, it is essential to identify various conditions using methods such as the inverse stability solution with frequency response function (FRF) to avoid chatter vibration effectively [7], multi-objective optimization considering natural

frequencies, stiffness, friction torque inside achieves 26% increased static stiffness of spindle-bearing system [8]. In addition, dynamic cutting force model with cutter stiffness was identified, and it has possibility to improve chatter vibration researches since chatter vibration is mainly influenced by system characteristics including stiffness change [9]. Also, the key point is about the change of dynamic characteristic of spindle system, which is generated by bearings inside since the bearing produces rotation and thermal effects on mechanical system including itself [10, 11].

A theoretical model has already been established for the change in properties of a milling system affected by the gyroscopic effect occurring in the spindle [12–14]. And one of researches suggested that time-varying stiffness system into fixed step time invariant could be used for the high speed spindle system with same theoretical model [15]. After that, the rotation effect on the shaft and bearings, which influences the stiffness, was investigated in accordance with various spindle speeds to show the change of FRFs compared to the static condition [16]. Also, the rotation effect on the micro milling process was suggested to predict chatter stability when using a simple geometrical model for micro milling [17]. The governing equations for chatter vibration prediction include gyroscopic effects and centrifugal forces exerted on the spindle system, especially for the support bearings [18]. Furthermore, in order to practically evaluate the effectiveness of these models, various experimental methods for the axial depth of the predicted cutting limit and the occurrence of chatter are continuously being studied. [19, 20]. To date, chatter analysis considering only the rotational effect of bearings has been actively conducted [21, 22], and results explain that the rotational effect of bearings will decrease the radial stiffness of spindle system from 5 to 15% on average. However, since the bearing continuously generates heat due to the spindle rotation, the characteristic analysis of the spindle considering only the rotation effect is insufficient to accurately analyze the milling stability.

High speed motorized spindle has complicated nonlinear and non-stationary features, but displacement-based model was reputed as one of notable solution to analyze thermal characteristic of the spindle [23]. Although thermal effects for chatter analysis were adopted after rotation theory, a thermomechanical model for a spindle-bearing system is well applied to stability analysis for the spindle-bearing system [24]. Research into the coupled heat generation relation between the bearing thermal expansion and the heat source change shows that the stable condition varies with the bearing thermal preload change [25, 26]. Also, the thermal effect induced by the relation between the workpiece and tool interfaces was found to affect the unstable cutting condition shift [27]. After several researchers identified that the thermal effect should be simultaneously considered with the rotational influence,

one study of the stability analysis for both effects depicted that the stable region could be changed within a 10% range given by the spindle operation [28]. Moreover, the cutting process considering the thermal effect increases the depth of the cut limit from 0.1 to 0.2 mm compared to static stable depth values [29]. This can be explained by the stiffness change in the spindle-bearing system, as the thermal expansion of the bearing causes a preload change with radial stiffness variation of 10–30% at the maximum increase ratio [30]. These results show that it is possible to increase the stiffness of the spindle system through thermal effects of bearings, which is directly related to the chatter stability enhancement.

Based on many researches, bearings have the greatest influence on the machining stability of the spindle system since it is rotating and has thermal effects. Hence, many attempts have been made to improve the accuracy of milling stability analysis such as the nonlinear spindle-bearing system modeling, thermomechanical model, or experimental verifications [31–36]. Currently, the thermomechanical dynamic model is widely applied to chatter stability analysis with experimental solutions [37, 38]. In addition, combination of tool-tool holder mode and spindle speed effect on this physical model were suggested and showed machining stability boundary change during milling process [39]. Commonly, studies depicting natural frequency values would be reduced 5–15% on average when the model only evaluates the rotational effect, and thermally induced factors are increasing the stability depth level by 10% at maximum. However, it is still necessary to verify the actual change and dominant parameters, such as a thermal time constant of the spindle, characterization methods including reliability of newly suggested tests. As described, thermal and rotational effects are critical factors for milling stability; however, experimental verifications about the non-stationary state of rotating spindle are insufficient to obtain accurate estimation.

This study investigates the effectiveness of the refined impact excitation to the non-stationary rotating spindle, particularly based on a coherence function of FRF during excitation. For the analytical approach, a thermomechanical model of the spindle-bearing system through simplification of major parameters is adopted, where the rotation and thermal effects of bearings are regarded as the major factors to analyze dynamic characteristics. In the experiments, three types of coupled spindle system are compared; thermal effect without rotation, rotation without thermal effect, coupled with thermal and rotation effects. FRFs obtained from refined impact excitation results are employed to draw respective SLDs, and the milling tests are carried out to evaluate the effectiveness of the SLDs obtained from the experiments, in which a

workpiece having a specific slope for continuous change in the axial depth of cut is used [40, 41].

## 2 Theoretical Background of Bearing Stiffness

### 2.1 Contact Angle Change with Rotational and Thermal Effects

In basic bearing analysis model, loads acting on the rolling elements or raceways in bearings are developed in only small and narrow regions at contact area between rolling ball and raceway. Hertzian theory demonstrates a relationship between load and deflection at the contact point as given by Eq. (1). According to the assembly conditions of bearing such as radial and axial fitting clearances, the contact angle readily changes, which eventually determines the friction heat as well as the initial stiffness of bearing as depicted in Fig. 1.

The combined load and ball center position are modified depending on the thermal deformation and the centrifugal force, which affects the system characteristics overall as shown in Fig. 1b. Due to the rotation effect, the contact angles at the outer and inner raceway are given by Eq. (2), which mainly affect the stiffness of spindle-bearing system.

$$Q = K\delta^{1.5}(Point\ loading\ of\ rolling\ bearings) \quad (1)$$

$$
\alpha_o = \cot^{-1}\left(\cot\left(\alpha_i\right) + \frac{F_c}{Q_{ia}}\right), or
$$
$$
Q_o = \left[1 + \left(\cot\left(\alpha_i\right) + \frac{F_c}{Q_{ia}}\right)^2\right]^{0.5} Q_{ia} \quad (2)
$$

The final geometric interference is equivalent to the new contact angle, changed with the summation of thermal deformation, and the total radial displacement based on the Love's displacement equation for the hollow shaft problem can be expressed as Eqs. (3) and (4), and the detailed derivations are referred to Wan C. and Harris T.A. [42, 43];

$$
\varepsilon_o = \frac{a_{t,o}}{3}\frac{(1+v_o)r_o}{r_o + r_h}\left[T_o\left(2r_o + r_h\right) + T_h\left(2r_h + r_o\right)\right], \varepsilon_b
$$
$$
= a_{t,b}r_b\Delta T_b, \varepsilon_{in} = \varepsilon_r + a_{total,i}r_i\Delta T_i \quad (3)
$$

$$\varepsilon_{total} = \delta_{total} = \delta_{rot} + \varepsilon_b + \varepsilon_{initial} + 0.5\left(\varepsilon_i - \varepsilon_o\right)\cos\left(\alpha_{th}\right) \quad (4)$$
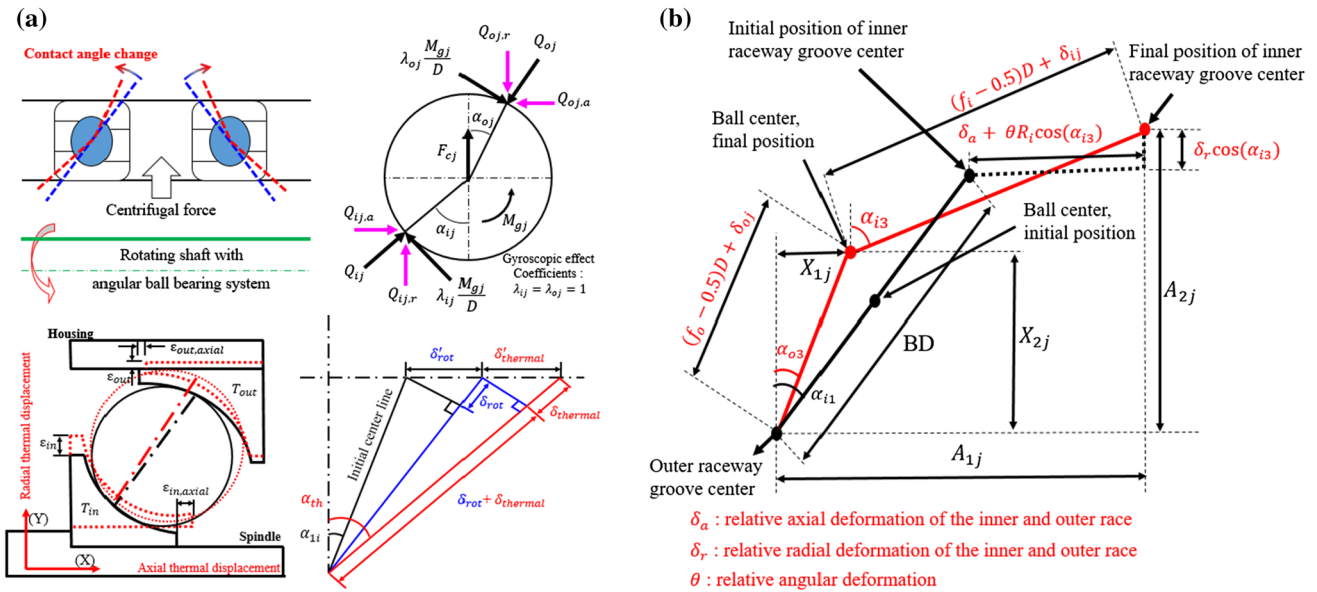
**Fig. 1** **a** Contact angle change of rolling element with raceways and **b** ball and raceway groove center point shift

## 2.2 Contact Stiffness and Bearing Heat

Rotational and thermally induced displacement inside the bearing is defined by the final contact angle. From Fig. 1b, the final location at each position ($A_1$) will be found with radial deformation between the location of groove curvature centers of each raceway ($A_2$), which consider the total deformation values at each position and angular location (5), and the ball center position (6), where $X_1$ is the projection of distance between the ball center and outer raceway curvature center and $X_2$ is the projection toward the radial direction:

$$A_{1j} = BDsin(\alpha_{th}) + \delta_{total,a} + \theta R_i cos(\psi_j), and$$
$$A_{2j} = BDsin(\alpha_{th}) + \delta_{total,r} cos(\psi_j) \tag{5}$$

$$\left(A_{1j} - X_{1j}\right)^2 + \left(A_{2j} - X_{2j}\right)^2 - \left[(f_i - 0.5)D + \delta_{ij}\right]^2 = 0, and$$
$$X_{1j}^2 + X_{2j}^2 - \left[(f_i - 0.5)D + \delta_{ij}\right]^2 = 0 \tag{6}$$

The inner and outer raceway deformation for calculating the inside ball location can assume that the ball gyroscopic moment is regulated entirely by the frictional force between the ball and outer raceway contact. Then, the given equilibrium of forces in the horizontal and vertical directions are explained respectively by the rotational and thermally induced forces where, $\alpha_{ij}$ and $\alpha_{oj}$ are equal to final contact angle $\alpha_{th,i}$, $\alpha_{th,o}$:

$$Q_{ij} \sin\left(\alpha_{ij}\right) - Q_{oj} \sin\left(\alpha_{oj}\right) - \frac{M_{gj}}{D}\left(\lambda_{ij} \cos\left(\alpha_{ij}\right) - \lambda_{oj} \cos\left(\alpha_{oj}\right)\right) = 0$$
$$Q_{ij} \cos\left(\alpha_{ij}\right) - Q_{oj} \cos\left(\alpha_{oj}\right) + \frac{M_{gj}}{D}\left(\lambda_{ij} \cos\left(\alpha_{ij}\right) - \lambda_{oj} \cos\left(\alpha_{oj}\right)\right) + F_{cj} = 0 \tag{7}$$

From this equation, the final inner and outer contact angles of each bearing are used for the determination of the final contact angle from the thermal terms. Also, the substitution of the above equations with the normal loads on balls, related to normal contact deformations, are as follows with coefficients equal to 1. Then, it is simplified using the force equilibrium assumption as follows:

$$\frac{\frac{\lambda_{oj}M_{gj}X_{2j}}{D} - K_{oj}\delta_{oj}^{1.5}X_{1j}}{(f_o - 0.5)D + \delta_{oj}} + \frac{K_{ij}\delta_{ij}^{1.5}\left(A_{1j} - X_{1j}\right) - \frac{\lambda_{ij}M_{gj}}{D}\left(A_{2j} - X_{2j}\right)}{(f_i - 0.5)D + \delta_{ij}} = 0$$
$$\frac{\frac{\lambda_{oj}M_{gj}X_{1j}}{D} + K_{oj}\delta_{oj}^{1.5}X_{2j}}{(f_o - 0.5)D + \delta_{oj}} - \frac{K_{ij}\delta_{ij}^{1.5}\left(A_{2j} - X_{2j}\right) + \frac{\lambda_{ij}M_{gj}}{D}\left(A_{1j} - X_{1j}\right)}{(f_i - 0.5)D + \delta_{ij}} - F_{cj} = 0 \tag{8}$$

Equations are rearranged with the gyroscopic moment and centrifugal force for rolling balls of angular contact bearing, where the deformed variables are evaluated from a numerical method such as Newton–Raphson. The input conditions are the axial force, radial force, moment, deformation or displacement values can be determined by force equilibrium. After obtaining the primary unknown quantities, the contact angle of each contact spot are as follows:

$$F_a - \sum_{j=1}^{j=Z} \left( \frac{K_{ij}(A_{1j} - X_{1j})\delta_{ij}^{1.5} - \frac{\lambda_{ij}M_{gj}}{D}(A_{2j} - X_{2j})}{(f_i - 0.5)D + \delta_{ij}} \right) = 0$$

$$F_r - \sum_{j=1}^{j=Z} \left( \frac{K_{ij}(A_{2j} - X_{2j})\delta_{ij}^{1.5} - \frac{\lambda_{ij}M_{gj}}{D}(A_{1j} - X_{1j})}{(f_i - 0.5)D + \delta_{ij}} \right) = 0$$

$$M - \sum_{j=1}^{j=Z} \left[ \left( \frac{K_{ij}(A_{1j} - X_{1j})\delta_{ij}^{1.5} - \frac{\lambda_{ij}M_{gj}}{D}(A_{2j} - X_{2j})}{(f_i - 0.5)D + \delta_{ij}} \right) R_i + \lambda_{ij}f_i M_{gj} \right] cos(\psi_j) = 0 \tag{9}$$

As a result, solutions for bearing stiffness are determined by the relation between the force and deformation for each direction with a summation of those for each ball position as Eq. (10) and the detailed derivations are referred to Harris T.A. and Hartnett M. [43, 44]:

$$K_a = \frac{F_{total,a}}{\delta_{total,a}}, K_r = \frac{F_{total,r}}{\delta_{total,r}} \tag{10}$$

Overall friction moment induced by the initial load is given by Eq. (11):

$$M_l = \left\{ 0.0262(0.5F_r + 0.44F_a)^{0.33} \right\}$$
$$\cdot \left\{ (0.9F_a \cot(\alpha_{1i}) - 0.1F_{rad}) \right\} \cdot d_m \tag{11}$$

In addition, friction moment caused by the lubrication can be considered as Eq. (12) depending on the lubrication type ($f_0$) [37]:

$$M_v = 10^{-7}f_0(v_{vis}S)^{2/3}d_m^3 \cdots [v_{vis} \cdot S \geq 2000]$$
$$M_v = 160 \cdot (10^{-7}f_0 d_m^3) \cdots [v_{vis} \cdot S \leq 2000] \tag{12}$$

## 2.3 Simulation Based on FEM Analysis

Through the theoretical approach for bearing stiffness change, rotation and thermal effects can be determined. To estimate the stiffness change caused by thermal expansion, thermostatic model of the spindle system is adopted. In Fig. 2a, 'Temperature measurement I' is monitored by a K type thermocouple, and its value is displayed on the CNC control panel, while 'Temperature measurement II' is for the spindle nose temperature measurement using same type thermocouple with a LabVIEW C-board (NI-9213, National Instruments Co.) (Table 1). Also, in order to estimate contact stiffness of interfaces, displacements of the tip of milling tool and the tool holder are compared to the static stiffness that are measured experimentally as depicted in Fig. 2c and Table 2. The HSC spindle used in this paper is commercially equipped in a 5-axis CNC machining center (Hwacheon M2-5AX), which is prepared to conduct cutting tests. In Table 1, basic properties of the spindle and bearing are listed.

As mentioned, simplified simulation spindle model was using input parameters for the calculation of temperature change of the spindle inside. In the simulation, the rotational speed from 0 to 18,000 RPM is applied to all rotating elements at 500 RPM intervals, and the heat generation of the bearing is calculated by the following equation derived from curve fitting method:

$$Heat\ generation = 2.04 \cdot 10^{-12} \cdot RPM^3$$
$$+ 4.96 \cdot 10^{-8} \cdot RPM^2 + 4.74 \cdot 10^{-5} \cdot RPM + 0.1 \tag{13}$$
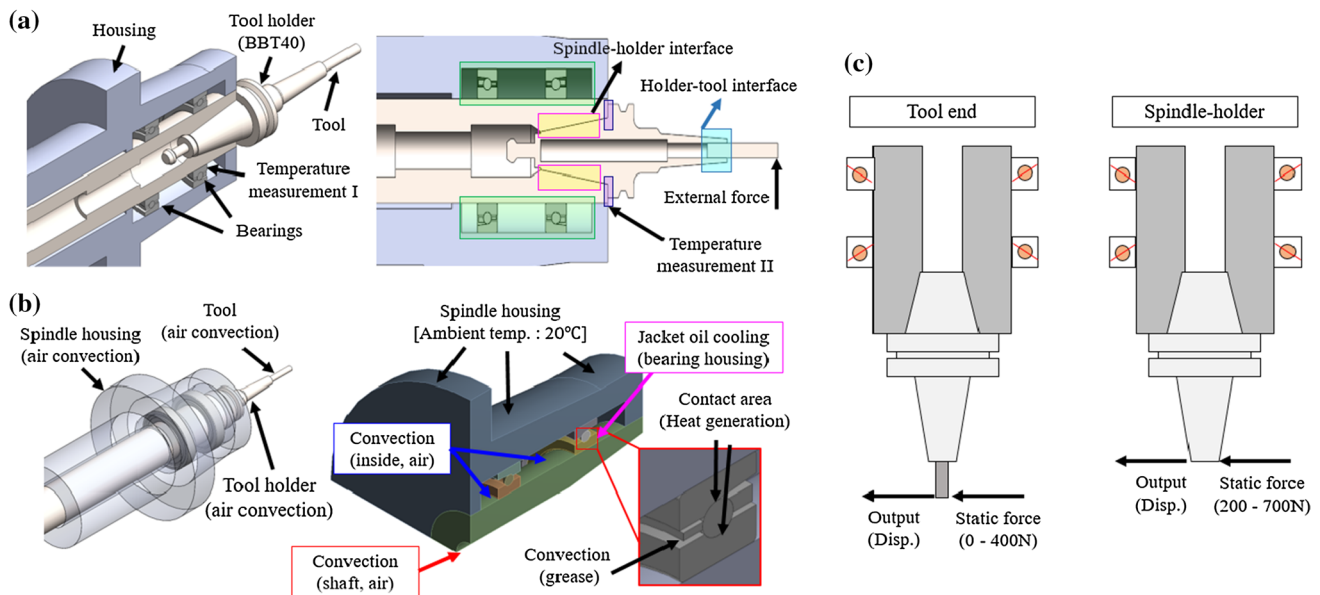


**Fig. 2** 3D FEM simulation model for **a** stiffness and **b** temperature of spindle inside, and **c** static stiffness measurement test

Heat flow is applied at the contact surface between raceways and balls, and convection conditions for the spindle system affect temperature changes, including ambient temperature. Bearing cooling mechanism is composed of jacket oil cooling on bearing housing and the oil mist lubrication inside. Also, convection conditions given by air on tool, tool holder, and spindle inside are considered as bearing cooling factors. Interface conditions among tool-holder-spindle are having a joint connection is assumed to be unchanged during operation, where the conduction is emerged based on the material property listed in Table 3. Convection is the main sink for heat generation of bearings, the input parameters and model are tuned until the errors between those values converge within 3%. Since the heat is generated by spindle rotation, it was set to the same speed in the heat generation calculation.

As a result, Fig. 3a shows the temperature change of the front bearing and spindle nose obtained through simulation and measurement test. Front bearing temperature of the simulation reaches 41.4 °C, when actual measurement value is 40.9 °C (1.1% error). The reason for this error is that the elaborate cooling system actually acting on the spindle is simplified into convection including bearing grease, air around shaft and housing. Since the error between the measured value of temperature change and the simulation result converged into 1%, it can be regarded as reasonable assumption to predict the internal temperature of the spindle based on the FEM thermal model simulation. Hence, based on this, simulation results of spindle inside temperature values were estimated as shown in Fig. 3b, c. In accordance with the spindle rotation speed, a trend of the maximum temperature value reached after a specific time was calculated.

**Table 1** Basic properties of the spindle and bearing

| Spindle | | Bearing | |
|---|---|---|---|
| Type | Commercial spindle | Type | Angular ball bearing |
| Bearing configuration | Back-to-back | Number of balls | 18 |
| Number of bearings | 3 (2 on front, 1 on rear) | Initial contact angle | 18° |
| Shaft diameter | 70 mm | Outer diameter | 110 mm |
| Taper (shank) | BBT40 (7/24 taper) | Bore diameter | 70 mm |
| Power | 18.5 kW | Ball diameter | 8 mm |
| Maximum speed | 20,000 RPM | Radius from ball center to inner race groove center | 39 mm |
| Spindle nose | Flat nose type | Radius from ball center to outer race groove center | 52.5 mm |
| Maximum feed speed (X, Y, Z) | 50,000 mm/min | Lubrication type | High-temperature resistance grease |
| Oil jacket cooling on bearing housing | 550 W | Kinematic viscosity of bearing lubrication | 20 mm/s |

**Table 2** Initial input parameters for stiffness simulation

| Parameter | Tool-holder interface | Spindle-holder interface | Tool-holder | Spindle-holder | Shaft-bearing |
|---|---|---|---|---|---|
| Stiffness (N/mm) | $20 \times 10^3$ | $60 \times 10^3$ | $6.3 \times 10^3$ | $28 \times 10^3$ | $39 \times 10^3$ |
| Damping ratio | 0.07 | 0.01 | 0.11 (tool) | 0.08 (holder) | 0.12 |

**Table 3** Material properties and convection coefficients for FEM simulation

| Material | Density (kg/m³) | Thermal conductivity (W/(m K)) | Thermal expansion coefficient (K⁻¹) | Elastic modulus (GPa) | Poisson's ratio |
|---|---|---|---|---|---|
| Ceramic (ball) | 3300 | 5 | $2.5 \cdot 10^{-6}$ | 300 | 0.23 |
| Resin (cage) | 1300 | 0.15 | $4.6 \cdot 10^{-5}$ | 0.375 | 0.2 |
| Structure steel (housing, shaft) | 7850 | 60.5 | $1.2 \cdot 10^{-5}$ | 200 | 0.3 |
| SUJ2 (raceway) | 7830 | 46 | $1.25 \cdot 10^{-5}$ | 220 | 0.35 |
| | Housing | Spindle inside | Bearings | Tool holder and tool | Shaft |
| Convection coefficient (W/m² K) | 25 | 150 (Air, rotation) | 300 (Lubrication, inside) 530 (Jacket oil cooling, housing) | 60 (Air, rotation) | 45 (Air, rotation) |
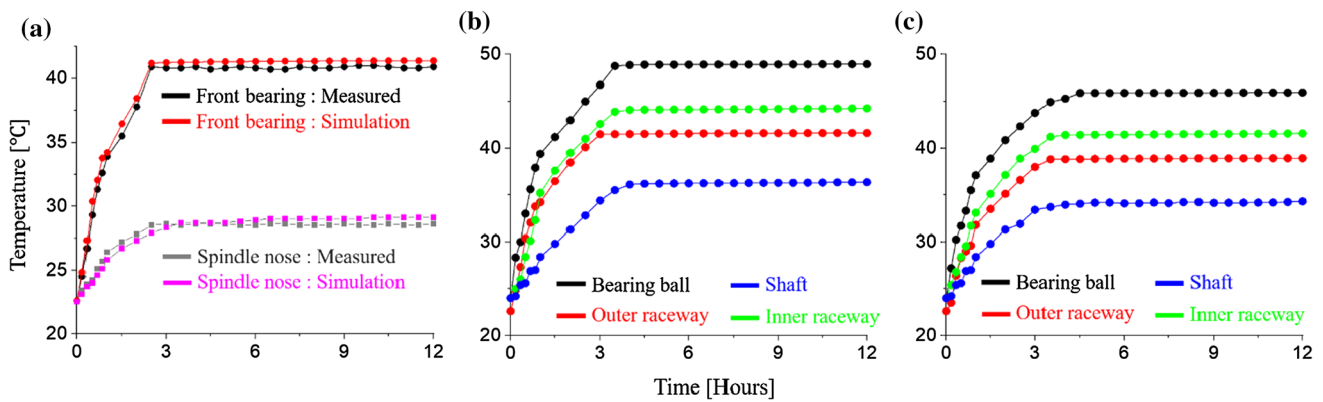
**Fig. 3** Temperature change of the bearing: **a** comparison between experiment and simulation results of 18,000 RPM rotation, **b** simulation result of 18,000 RPM and **c** simulation result of 12,000 RPM

**Fig. 4** Contact angle change calculated by theoretical approach: **a** inner race **b** outer race
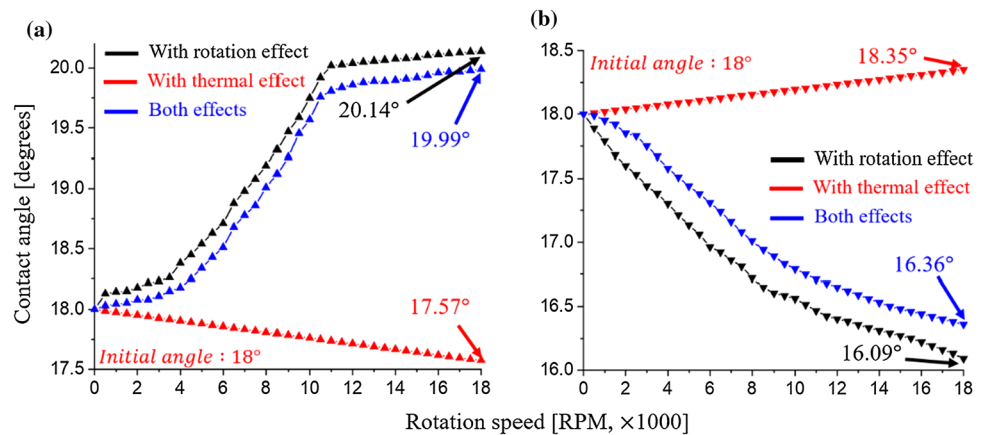


The temperature change results from the FEM simulation are substituted to the theoretical Eqs. (3) and (4) for thermal deformation, so that the contact angle change caused by rotation and thermal effects could be calculated as shown in Fig. 4. Contact angle changes are depicted following rotation speed orders, where the spindle speed is replaced by the heat generation of the contact region between the balls and raceways of two support bearings. Figure 4a shown increased contact angle between balls and inner race, and Fig. 4b shows reciprocal result. Input parameters and properties of bearing are inserted into MATLAB to calculate total load 'Q' on rolling elements with contact angle change obtained from the simulation result. Final deformation of each bearing part is also computed considering rotation and thermal effects induced by certain rotation speed, 18,000 RPM at maximum. The bearing stiffness according to rotation speed was used in the spindle model, and the system stiffness change caused by rotation and thermal effects was derived.

The stiffness can be estimated based on the result reflecting this phenomenon as expressed in Fig. 5, interface stiffness (Fig. 5b) values calculated through iterative simulation process using FEM model, hence static values at zero rotation speed are same with the experimental measurement process measured from Fig. 2c test setup. The results are clearly appeared in two ways: the decrease in stiffness due to the rotation effect and the increase in stiffness affected by the bearing thermal effect depicted in Fig. 5a–c. The reduction in stiffness is not noticeable in the low-speed range where it increases up to 3000 RPM, as the rotation speed increases up to 10,000 RPM, a sharp decrease proceeds. The deformation amount of the bearing balls and rings increases linearly under the influence of centrifugal force and moment, but the stiffness change is reduced when the system reaches a certain rotational speed. It appears that the rotational influence on bearings is diminished by the fixed spindle housing and the shaft element expanding by rotation. As mentioned previously, higher stiffness is one of essential parameters to improve maximum/minimum performance or stability of spindle system. Based on stiffness graphs, it suggests that bearing thermal effects will produce better stable machining condition since stiffness is increased from rotation effect of spindle system.
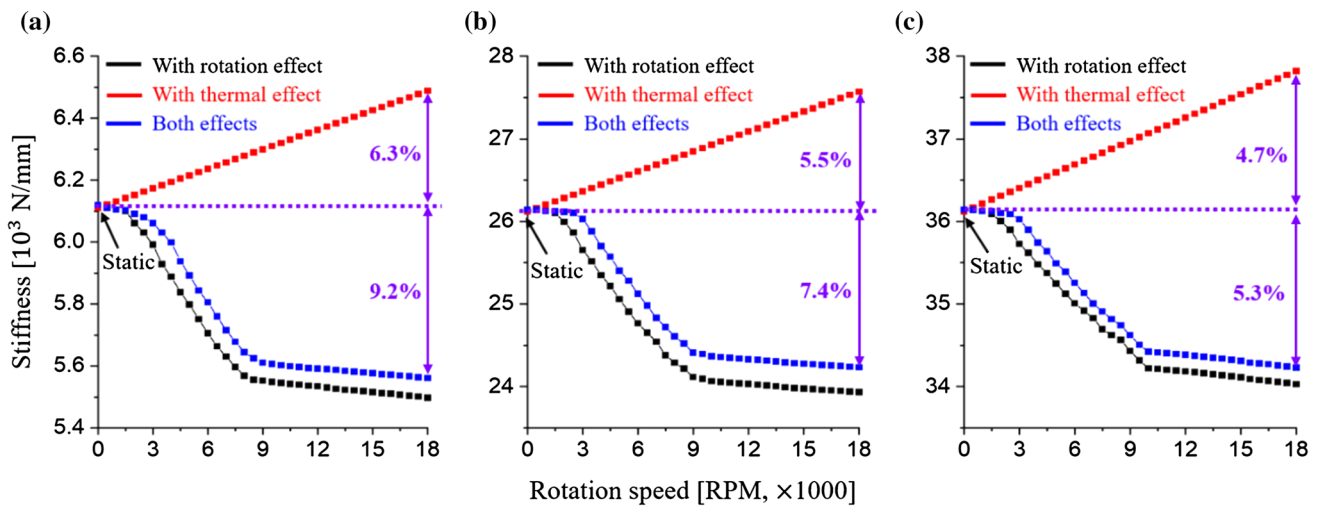
**Fig. 5** FEM simulation results for stiffness at: **a** tool end, **b** tool holder-spindle interface, and **c** end point of the shaft-bearing assembly

# 3 Characterization of Spindle-Bearing System

## 3.1 Impact Excitation

In Fig. 6, vibration signals were measured using the accelerometer (ICP® 352A21, PCB Piezotronics), with the impact force applied at the tip of the dummy tool given by the impulse hammer (ICP® 086C03, PCB Piezotronics). When controlling the other disturbances caused by a difference between the real and dummy tool, the existence of the tool flute is the only disparity in the given tests. Both data sets were acquired using a LabVIEW board (USB6363, National Instruments Co.) given by the experimental conditions listed in Table 5. For evaluating the rotational and thermal effects, a noncontact sensor (Capacitance type, 5810 system, ADE Technology) was used instead of the acceleration sensor.

Thermal effects of spindle bearings were investigated using the conventional impact hammer test at the state of temporary stop. Rotation effect was measured during the spindle rotation and it readily generate noise signals as well as frequency deviation. To securely acquire the FRF, coherence functions described in below were cautiously monitored.

$$Coherence\ function = \frac{|G_R(f)|^2}{G_I(f) \cdot G_O(f)} \quad (14)$$

Namely, coherence function could be regarded as the correspondence between excitation and response signals when the spindle system is exerted to the input signal, and it could
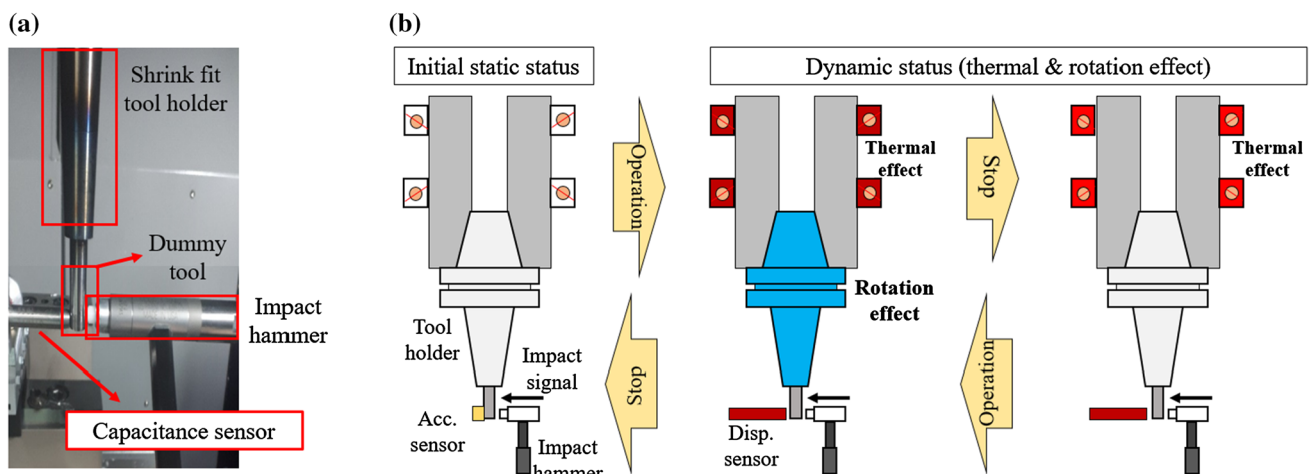


**Fig. 6** **a** Impact excitation test for rotating spindle and **b** schematic diagram of the whole test process

demonstrate two states: response has anti-resonance points where vibration responses are very low after it encounters structural resonance points, and excitation force was not exerted well to regulate the relation between the impulse force and tool vibration. Moreover, there are essential factors to be considered in order to evaluate the effectiveness of refined impact hammer tests for rotating spindle system, which is indicated as a flow diagram depicted in Fig. 7.

Based on the process of coherence check, Fig. 7 depicts that the reference response gained from conventional impact hammer process is necessary to compare the result of rotation system. Also, it needs to check the time interval between impulse points while the residual vibration generated by previous impulse signal could have an effect on present vibration signal. The time it takes to rise to the peak value of the impulse force and the noise are the processes for verifying the accuracy of the input signal, where those are determined by the reference impulse force signal obtained from the stationary condition.

In Table 4, major factors for coherence check are listed. First consideration factor of refined impact hammer test method is about impact point exerted on rotating tools (Exp. T-1). When the tool is rotating, a slip will be generated between the impact hammer tip and the surface of rotating dummy tool. Then, the input signal for system response is deviated as shown in Fig. 8. The bad impact position provides incomplete input signal, then the results reveal lower coherence at specific frequency as well as noise in high frequency band because incidental impulse peaks are included by friction between the hammer tip and tool. This disturbance could be minimized through observing coherence function and choosing the impact position.

Furthermore, the false response (300 Hz) caused by the spindle run-out was removed using filtering method. On the other hand, the weak impulse force produces noise response particularly in the high frequency band because of the contact joint of tool-clamp-shaft. From the results of different exciting forces, at least 200 N of impulse magnitude was required to obtain high level coherence function in this system as shown in Fig. 8a. When the spindle is rotating, to overcome the slip problem between the hammer tip and dummy tool, sufficiently larger impulse magnitude
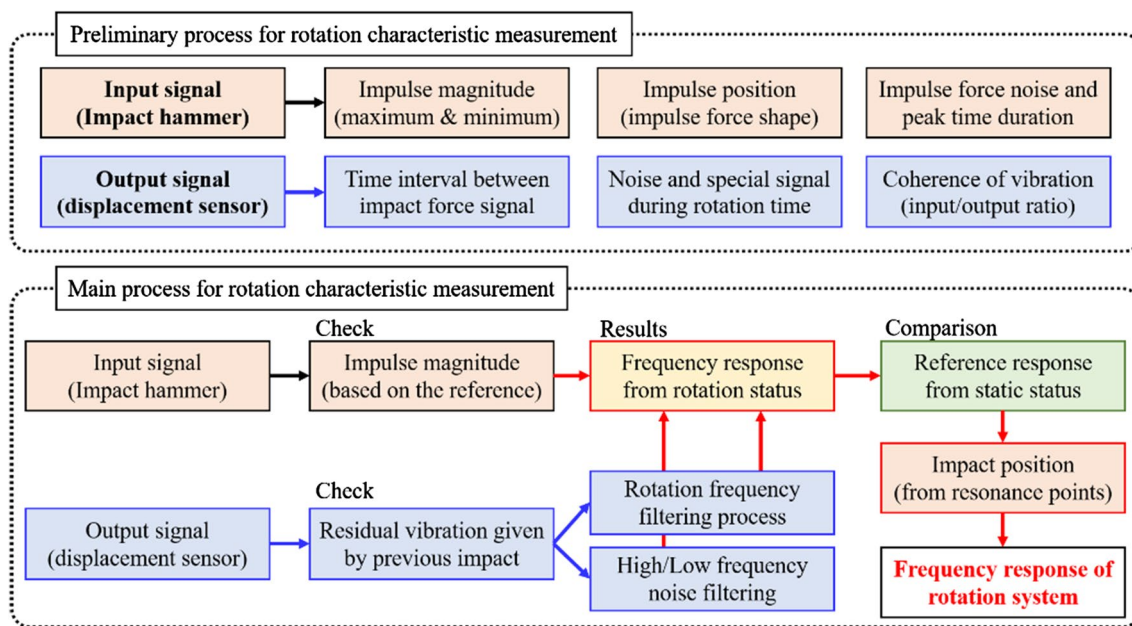


**Fig. 7** Flow chart of coherence check process for rotation spindle-bearing system

| Table 4 Test conditions for refined impact hammer test verification | Test factor | Impulse force magnitude | Rotation signal filtering | Impact position | Rotation speed |
|---|---|---|---|---|---|
| | Exp. T-1 | 300 (± 10%) N | With filtering | Bad position Best position | 18,000 RPM |
| | Exp. T-2 | 300 (± 10%) N | Without filtering With filtering | Best position | |
| | Exp. T-3 | 50, 100, 200, 300 N | With filtering | Best position | |
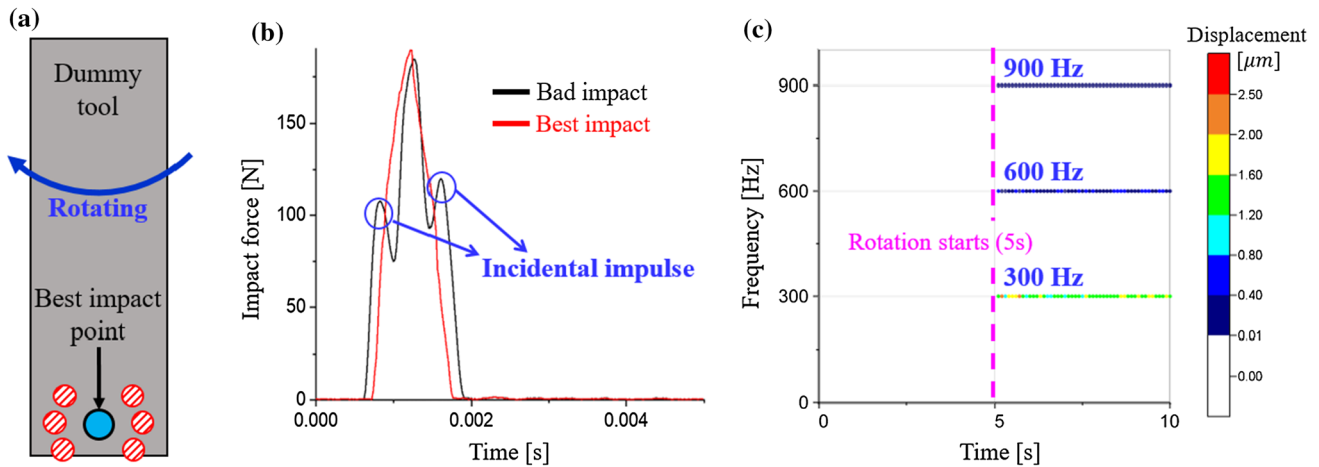
**Fig. 8** **a** Impact points on tool tip, **b** impulse amplitude and shape given by impact point, and **c** specific noise signal induced by rotation

is necessary. In Fig. 8b, frequency response results were derived from various impact hammer tests with different impulse force amplitude. In order to gain higher coherence of frequency response, impulse amplitude should be reaching at least 200 N. In the case of 50 N force, resonance frequencies after first range are removed or shifted. Because the frequency response is essential to derive the milling stability lobe diagram, uncertain information caused by lower impulse force should be avoided. In addition, the lower amplitude of impulse forces such as 50 or 100 N was not able to measure the system response after 2.5 kHz. In accordance with rotation speed of the spindle, repetitive noise or disturbance in specific frequency value can be included in the displacement sensor as shown Fig. 8c. They are generated by the runout of tools. But it is simply solved by the information of system characteristic using the conventional method. In order to avoid false resonance point generated by spindle

rotation speed, FFT filtering at the frequency corresponding to spindle speed is adopted.

Refined impact hammer tests on the rotating spindle can be applied to provide dynamic characteristics of rotating spindle-bearing system. In Fig. 9a, the average value of the highest coherence signal was obtained above 0.98 (not exceed 1 since '1' means the perfectly matched coherence), and it was confirmed that the anti-resonance point decreased to 0.58 of the lowest average value. In order to maintain the coherence of measurement results, impulse point screening process based on impulse signal analysis is conducted. At the same time, impulse signal amplitude determines useful cases for frequency response calculation. And filtering for rotating signal and high frequency noise is accompanied to gain proper frequency response results as shown in Fig. 9b.

In the characterization process, at the first stage, the impulse was exerted on the stationary spindle at the tool
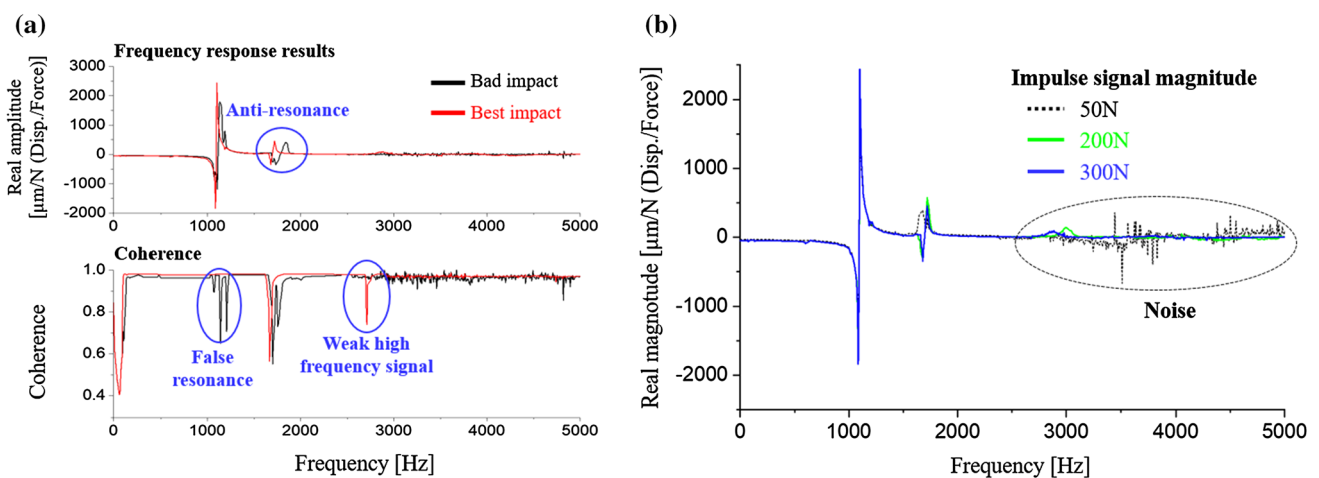


**Fig. 9** **a** Coherence check with frequency response results, and **b** test results under different impulse force magnitude

end. After that, the impulse was exerted on the rotating tool end, which was repeated in accordance with the operation time with setup conditions listed in Table 5. Therefore, to measure the thermal effect, the spindle is shortly stopped after each specified operation time. When the spindle FRF is kept unchanged after certain operation time, that specific operation time is set as a thermally stable period.

In the test, the dummy tool was adopted by considering the mass and length effects given by the discrepancy between the real milling tool and dummy itself and when the characteristic does not change even if the rotation of the spindle continues, it is considered as the thermally steady condition. Although the real tool produces the most accurate characteristics, sharp edge may cause impulse errors. From Fig. 10a, the thermal time constant of the spindle could be derived from the shift trend of frequency response. The spindle was stopped temporarily every hour to measure the FRF influenced by the thermal effect. It is clear that, as the operation time increases, the resonance frequency shifted toward

right, which means the stiffness increases. After the spindle operation time reaches 3 h, there is no change in the characteristics of the spindle due to the thermal effect. Therefore, the thermal effects increase the stiffness as expected from Sect. 2, and 3 hours of operation needed for the minimum saturation for the spindle condition.

In Fig. 10c, d corresponding to the first and second resonances of Fig. 10b, due to the rotational effect of bearings, the rigidity was lowered and the resonance frequency was decreased. The thermal effect of bearings increases the resonance frequency as like compensation of the reduced stiffness, but it has a lower value than the resonant frequency of the stationary condition. In Table 6, the larger shift of the resonance frequency is observed in high frequency bands, but the vibration magnitude becomes significantly lower than the first resonance. Chatter vibration has a frequency nearby natural frequency of a system [1] since structural FRFs are dominantly related to chatter occurrence. Hence, chatter vibration generated near the first resonance frequency

**Table 5** Impact hammer test setup conditions

| Tool | Tungsten carbide, φ10 (Dummy tool) | Impact force | 300 N (± 10%) |
| --- | --- | --- | --- |
| Tool holder | BBT 40 shank, Shrink fit tool holder | Sampling frequency | 50 kHz |
| Overhang | 45 mm | Sensor | 1. Acceleration sensor<br>2. Capacitance sensor |
| Status | 1. Stationary<br>2. Rotating (1, 2, 3, 4 h) | Weight of sensor (acceleration) | 0.002 kg |



**Fig. 10** Impact excitation test results: **a** thermal time constant test, **b** impact hammer test results of all cases, **c** first resonance area around 1100 Hz, and **d** second resonance area around 1750 Hz
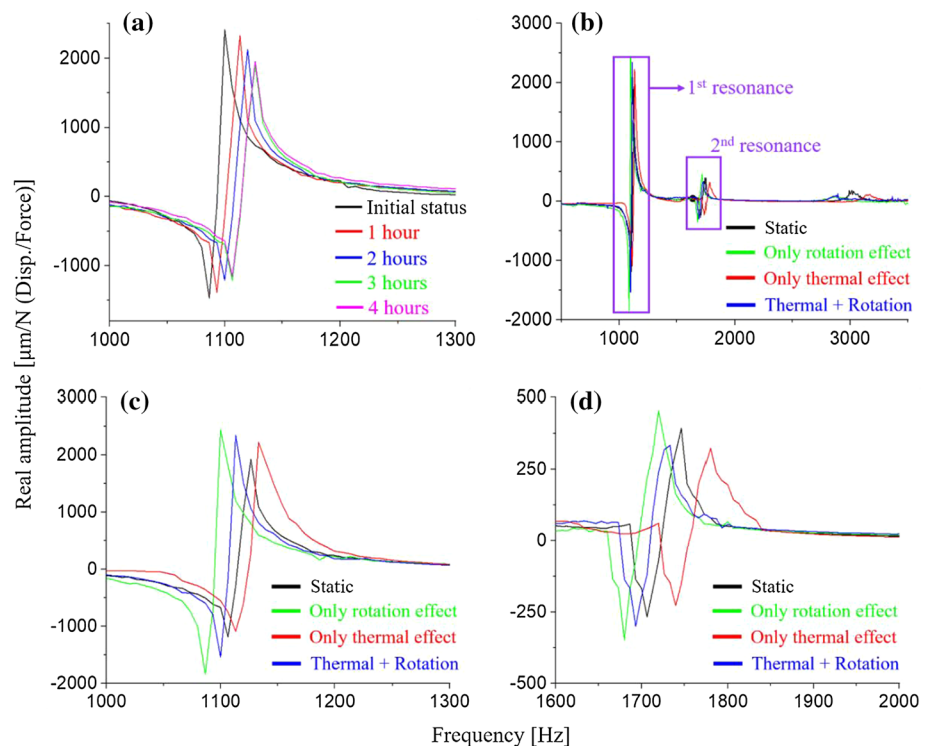
**Table 6** Resonance frequency values of each impact hammer test result

| Resonance | Stationary (Hz) | Only thermal effect (Difference onto static) | Only rotational effect (Difference onto static) | Both effects (Difference onto static) |
|---|---|---|---|---|
| First | 1125 | 1135 Hz (0.8% increase) | 1095 Hz (2.6% decrease) | 1110 Hz (1.3% decrease) |
| Second | 1735 | 1780 Hz (2.6% increase) | 1725 Hz (0.5% decrease) | 1745 Hz (0.5% increase) |
| Third | 3000 | 3160 Hz (5.3% increase) | 2870 Hz (4.3% decrease) | 2885 Hz% decrease) |



**Fig. 11** SLD derived from FRF of experimental and simulation method: **a** SUS303 case, **b** major area for the SUS303 case
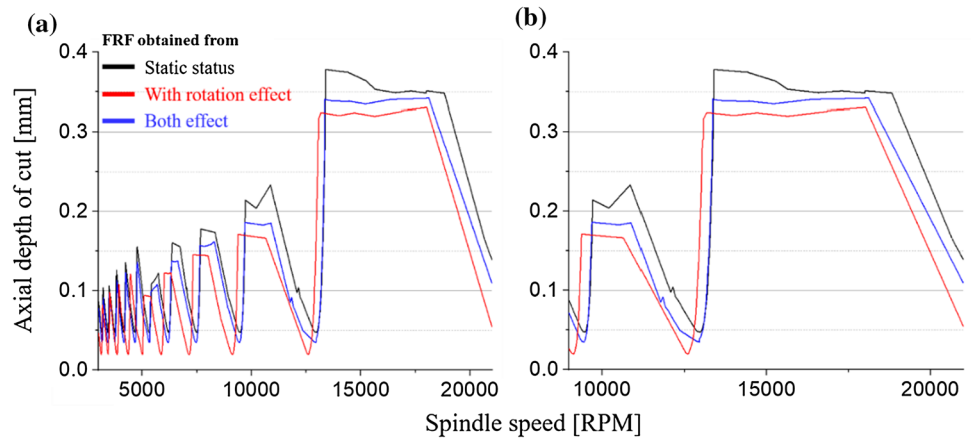
of spindle system will have the highest magnitude among chatter vibration components. Based on the test results, the chatter component will have the highest amplitude level around 1.1 kHz (first resonance frequency value of spindle system) and the lowest amplitude after 2.8 kHz. In addition, owing to the stiffness increase, the thermal effect of the bearing is expected to reduce vibrations generated during machining.

## 4 Stability Lobe Diagram and Machining Conditions

### 4.1 Stability Lobe Diagram (SLD)

It is difficult to exactly solve the nonlinear relation for the cutting mechanism, so it is necessary to approximate it as a linear form to obtain a solution for the stable machining conditions. In order to predict the actual cutting situations, frequency responses considering rotational and thermal effects are applied to obtain the SLD shown in Fig. 11. As rotation effect of bearings generates stiffness drop, stable cutting conditions will be decreased when it is compared to the reference lobe obtained from impact hammer test of the stationary spindle. And stiffness increase given by thermal effect of bearings is reflected to SLDs as the compensation of stable machining area, critical depth of cut moves upward compared to the case of rotation effect.

**Table 7** Minimum depth of cut limit for the SUS303 case

| | Experiment (Stationary) | Experiment (Rotation effect) | Experiment (Both effects) |
|---|---|---|---|
| Depth of cut (mm) | 0.047 | 0.019 | 0.035 |

The major difference in SLDs is clearly depicted in Fig. 11, and when the rotation effect is applied, the minimum limitation of the axial depth decreases as much as 7.4% on average. In addition, in Fig. 11b, it increases to 10.3% while the spindle speed change is also observed corresponding to same axial depth. Only the case considering the rotational effect had the lowest stiffness, resonance frequency, and vibration amplitude, which were associated with the critical depth shown in Table 7. Usually, minimum depth of cut value in SLD is sunken area of graph, and the zone under this value would represent stable depth of cut for corresponding spindle system. For instance, stiffness decrease of bearings can be interpreted as stable depth reduction, since SLD is calculated from FRF ("Appendix 1"). In conventional SLDs, the conditions for maximum performance of the high-speed spindle are determined based on the stationary condition of the system. Consequently, the cutting depth where chatter vibration occurs does not reflect the dynamic characteristics of spindle-bearing system. In order to predict chatter vibration accurately, the shift of the SLD should be carefully observed according to the spindle rotation speed,

even though the stable area gets larger due to the thermal effect of the bearing.

## 4.2 Machining Experiment

The machine tool in the experiments was the 5-axis CNC machining center, Hwacheon M2-5AX, with a spindle power of 18.5 kW, a max speed of 20,000 RPM, and BBT 40 for tool fixture. Cutting forces were measured using a Kistler type 9257B dynamometer and a LabVIEW device with 50 kHz sampling frequency. The surface roughness was measured by a contact-type surface tester (SURFT-EST® SJ-410, Mitutoyo) with 2.5 µm window size, and the status of tool marks induced by chatter vibration were observed by digital microscope (Dino-Lite, AM4815 series, ANMO Corp.). Basic conditions for tests are listed in Tables 8 and 9 presents the cutting conditions. In Fig. 12, a workpiece with a slope will produce a changed

axial depth of cut in feed direction, and chatter vibration will cause large portion of cutting force increase if the spindle reaches critical axial depth value.

The effect of tool wear or breakage on chatter vibration should be minimized to compare only the effect of bearings; hence, it was fixed at 0.01 mm/tooth for all conditions, as shown in Table 9. Feed per tooth value might be extremely low for the 10 mm milling tool, but this prevents tool damage and reduces factors other than bearing effects. Also, each cutting test is conducted by the new tool without any damages on it to maintain initial condition. For the thermal effect observation during the end milling process, the pre-operation time was set as 3 h before cutting each workpiece in order to proceed with next machining. It reduced the temperature through a cooling time of at least one day. To refrain the tooth passing frequency and its harmonics from encountering chatter frequencies, rotation speed conditions are selected as shown in Table 9.

**Table 8** Basic conditions of the cutting tests for SUS303

| Tool (mm) | $\phi$10 Tungsten carbide 2 flutes, square end mill without wear | Pre-operation time for thermal effect | 3 h |
|---|---|---|---|
| Tool holder | BBT 40, shrink fit tool holder | Milling type | Dry & Slotting (Radial depth: 10 mm) |
| Overhang (mm) | 45 | Pre-operation time for thermal effect | 3 h |

**Table 9** Experiment numberings with cutting conditions

| Workpiece material and pre-operation time | Experiment number | Spindle speed (RPM) | Feed rate (mm/min) | Feed per tooth (mm/tooth) |
|---|---|---|---|---|
| SUS303: A, B, C -1: No pre-operation -2: 3 h pre-operation | Exp. #A-1, 2 | 18,000 | 360 | 0.01 |
| | Exp. #B-1, 2 | 15,000 | 300 | |
| | Exp. #C-1, 2 | 12,000 | 240 | |



**Fig. 12** Schematic diagram for machining experiment setup with Kistler type 9257B dynamometer
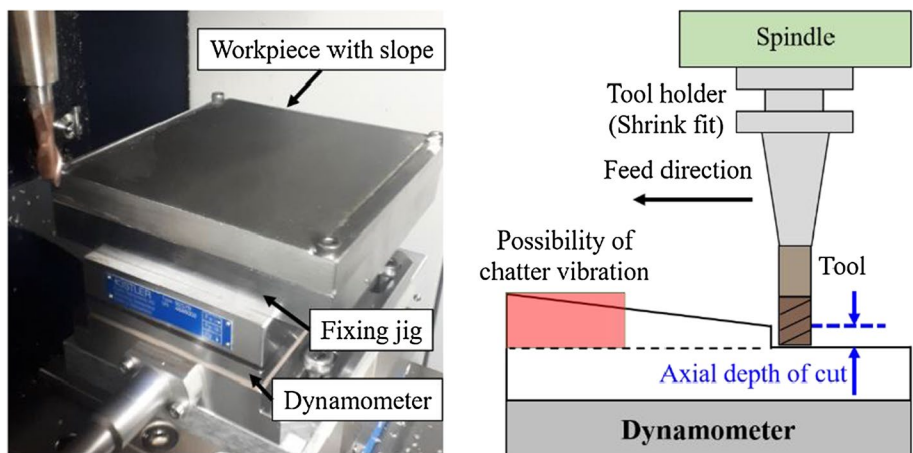
## 4.3 Results of Cutting Tests: SUS303

Previously, the coherence calculation of impact hammer tests for rotating spindle system shows that refined method can be available to predict SLDs considering dynamic characteristics of spindle-bearing system. However, if machining experiment results do not match with SLDs, coherence check process may not prove the reliability of refined impact hammer tests. In order to examine the effectiveness of refined tests and SLDs, critical axial depth of cut at the chatter occurrence points should be matched to predicted values, which will be investigated in two terms: chatter frequencies and surface roughness. Chatter frequencies are generated after the spindle exceeds the axial depth limit during milling process, and surface roughness will indicate abrupt changes from chatter occurrence area.

In the case of 18,000 RPM, depicted in Fig. 13, there are particular features to detect the chatter vibration during the end milling process. At first, when the milling tool goes in the feed direction, the cutting force increases in a linear relationship with axial depth of cut changes. Second, when the force signal reaches the chatter occurrence limit, abrupt signal peak points are periodically generated in the time domain, resulting in chatter oscillations around the resonance frequencies acquired from experimental method. The chatter frequency corresponding to the first resonant frequency has the highest chatter vibration amplitude, while second and third components have lower values in order, since the first resonance is determined by the tool and tool holder interface or tool end where the cutting forces are

applied dominantly. And, tooth passing frequency component is escalated constantly since the cutting volume is increased at the same time. However, since cutting force signals are not showing specific trend in accordance with chatter development, it is hard to determine the chatter only by the tooth passing frequency amplitude.

Table 10 and the dotted lines in Fig. 13 indicate that the rotational effect of the bearing is compatible with the actual cutting situation, and the chatter starts notably after the critical axial depth of cut. Difference of chatter occurrence limit observed in the rotation effect and the both effects could be explained by thermally stable period. This result verifies that the refined impact hammer tests are effective for predicting actual stability conditions, even including thermal effect of bearings. Each chatter frequency has an error of 1–3%, which seems to be caused by the change of the interfaces or the difference of each tool. Also, since the chatter frequency does not have the same frequency value as the resonance frequency of the system, each component has an error of 1 to 2% with the resonance frequency.

From the surface measurement, it is possible to observe notable tool marks from the point of the chatter borderline compared to the normal cutting condition. For instance, Fig. 14c depicts that measurement point after the chatter vibration has severe tool marks when it is compared to other two measurement results. It would be appeared certainly as the surface roughness difference induced by the thermos-elastic effect is shown in Fig. 15. As listed in Table 10, critical axial depth values of rotation cases are 10.2% lower than depth values of both cases, which is



**Fig. 13** Cutting force analysis results for without thermal effect using SUS303: time-domain data for **a** Exp. #C-1, **b** Exp. #C-2 and FFT for **c** Exp. #C-1, **d** Exp. #C-2
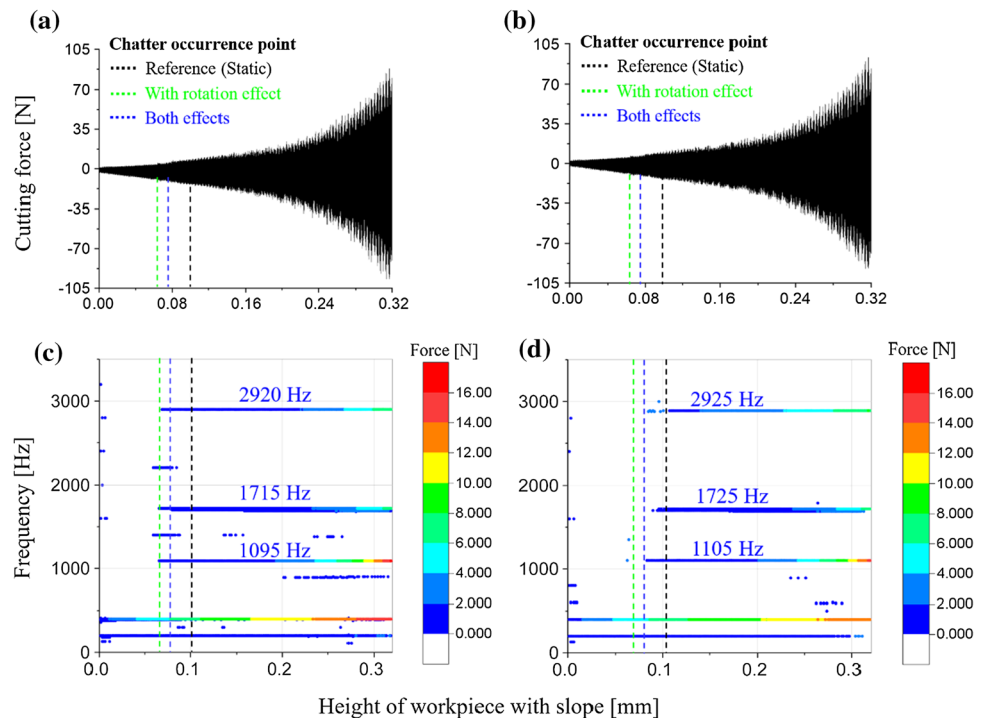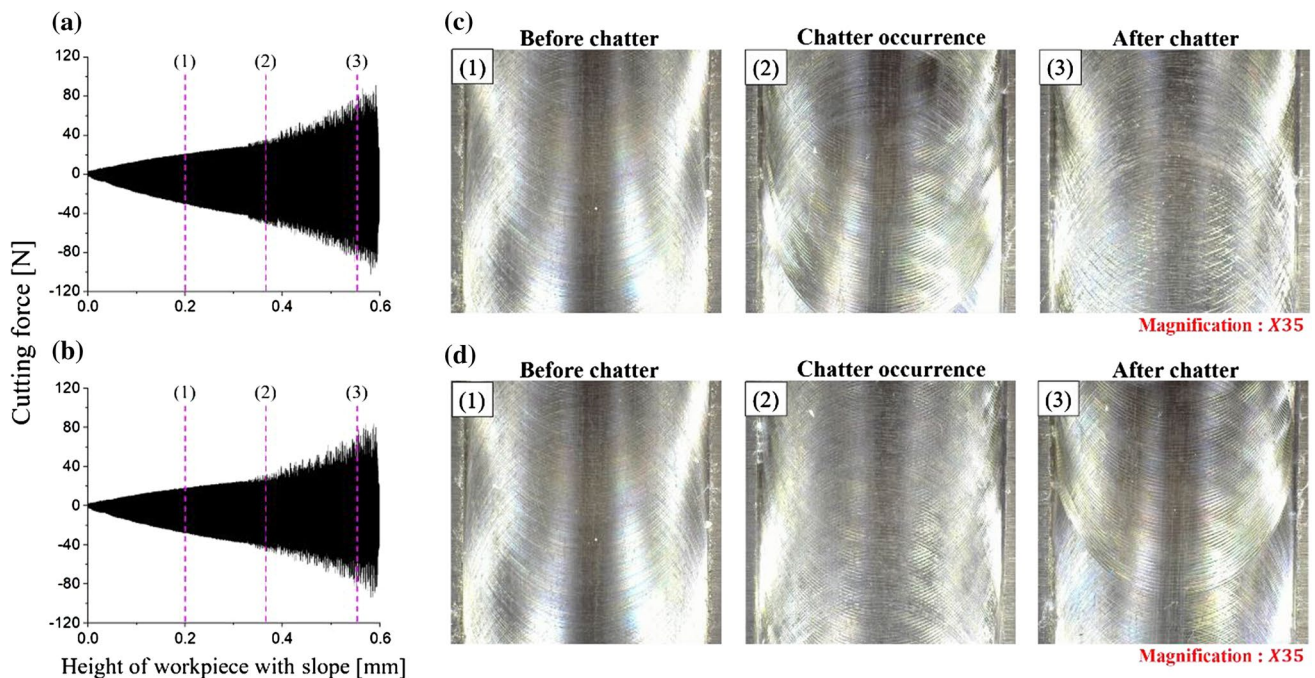
**Table 10** Axial depth of cut values at critical stability point of SUS303

| Rotation speed | From impact hammer test (mm) | | |
|---|---|---|---|
| | Static | Rotation | Rotation and Thermal (Both) |
| 18,000 RPM | 0.351 | 0.331 | 0.342 |
| 15,000 RPM | 0.367 | 0.317 | 0.336 |
| 12,000 RPM | 0.106 | 0.062 | 0.076 |

| From cutting tests (mm) | | | | | |
|---|---|---|---|---|---|
| #A-1 (Rotation) | #A-2 (Both) | #B-1 (Rotation) | #B-2 (Both) | #C-1 (Rotation) | #C-2 (Both) |
| 0.333 | 0.344 | 0.315 | 0.338 | 0.065 | 0.078 |



**Fig. 14** Non-stationary signal of **a** Exp. #A-1, **b** Exp. #A-2 and surface status of **c** Exp. #A-1, **d** Exp. #A-2

caused by stiffness change of the bearing thermal effect. It is hard to distinguish chatter occurrence points from time domain signals in Fig. 14a, c, but Fig. 14d shows that tool marks are less severe than Fig. 14b. Notable result is depicted in Fig. 15b, which is comparing the results of Exp. #C, and showing that chatter occurrence depth is increased as much as 20%. The point at which the rapid change in surface roughness occurs obviously corresponds with the starting time of axial depth to generate chatter vibration, and since then, the surface roughness is increases. Once chatter vibration occurs, the surface roughness increases more than 11% compared to the normal condition. And thanks to the bearing stiffness compensated by the thermal effect of bearing, increase of surface roughness after the chatter was regulated by 3.7%

on average. Based on the experiment results, minimum machining performance in stable cutting conditions are enhanced by thermal effects of spindle-bearing system owing to stiffness increase.

Through the experiment results, the actual cutting tendency could be projected properly by adopting a refined impact hammer test on the rotating spindle even though small deviations exist. The critical axial depth of cut difference predicted through experiments had a low error rate compared with the actual machining results. From Table 10, the average deviations in critical axial depth between stability lobe and the actual cutting test were 1.9%, and 1.2% for both effects. The refined impact hammer tests can predict machining conditions considering chatter vibration during milling process within 2% error rate.

**(a)**

**(b)**
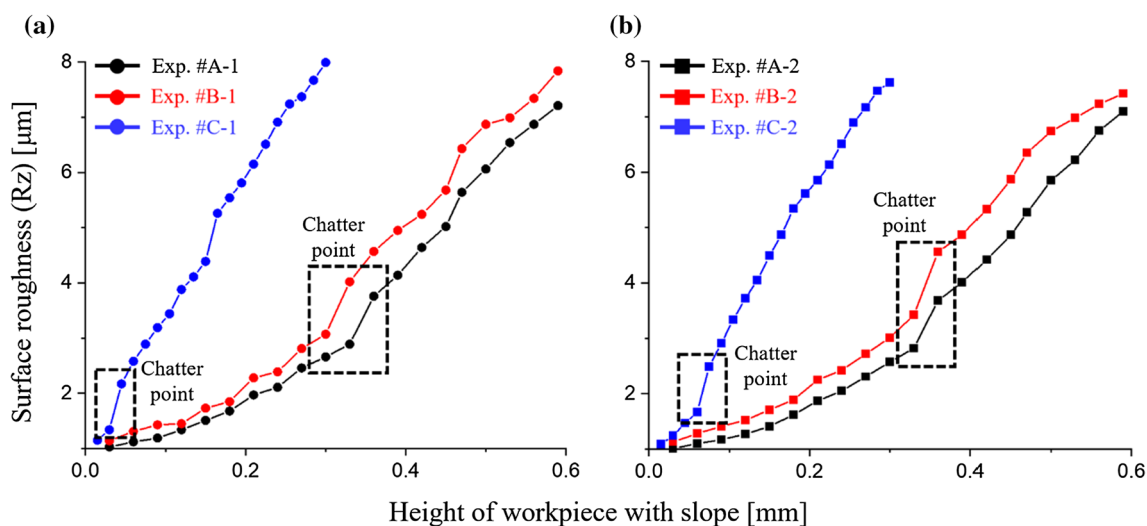
Fig. 15 Surface roughness values (Rz) measured after cutting tests (SUS303): **a** without thermal effect, **b** 3-h pre-operation

## 4.4 Discussion

In previous researches [32, 35], conventional methods have been adopted for characterization and it only reflect that the responses of the static spindle-bearing system. Meanwhile, refined method includes response of the dynamic condition (rotation, thermal effects) accompanying with coherence check for the test reliability. Results depict that thermal effect of inside bearings will increase the stiffness measured at tool end as much as 3.7% on average, which is directly related to machining stability. From the experimental results, maximum improvement of axial depth limit was 20% since system stiffness is enhanced by thermal effect of bearings as shown in FRF results. In addition, coherence check process removes unnecessary signals in order to draw precise SLDs. In previous investigation [40, 41], the experimental identification of SLDs was conducted on workpiece surface and cutting force analysis in frequency domain, which perfectly reflected practical milling situation. However, it does not compare difference of SLDs induced by thermal effects since thermal influence would be generated after specific operation time of spindle. This research certainly suggests that thermal effects induced by mechanical parts of spindle-bearing system should be considered in characterization process with adopting refined method.

Consequently, improved SLDs given by refined impact excitation tests can accurately predict the limitation of the axial depth of cut in the practical machining operation while it presents dynamic characteristics of spindle-bearing system. Also based on spindle feature changed by thermal effect of bearings, the axial depth limit at chatter point is sufficiently corresponding to the actual axial depth of cut limit.

## 5 Conclusion

In this study, machining stability was investigated through SLDs with consideration of the rotational and thermal effects of the spindle-bearing system. In the analytical approach, the bearing stiffness corresponding to the contact angle change was determined, as both the centrifugal force and thermal deformations of the elements were considered. At the same time, in order to reduce the complexity of the system, suggested analytical model of the spindle-bearing was applied to simplify nonlinear or uncertain parameters.

In the experiment, suggested refined impact excitation test method was applied to reflect both rotational and thermal effects. Through observing the coherence functions and adopting signal filtering method, the influences of disturbances such as the slip between tool and hammer tip, the effect of run-out and the weakness of impulse magnitude were remarkably minimized. Through the simulation and an impact excitation test, it was shown that the rotational effect decreases stiffness while the thermal effect increases stiffness. Due to the stiffness change induced by spindle operation, stable cutting conditions are reduced after a short operation time of the spindle, while it is increased 10% to 20% after longer operation time accompanied by the thermal effect.

Next, SLDs using frequency responses obtained from all processes were created and evaluated using cutting tests. A stability check based on the bearing rotation effect was well matched with the actual chatter occurrence points when tested without pre-operation. On the other hand, pre-operation case accompanying thermal effect agreed with the stable depth of cut calculated from an examination of all the bearing effects. As a result, conventional impact hammer test could be substituted by refined methods in order to apply the
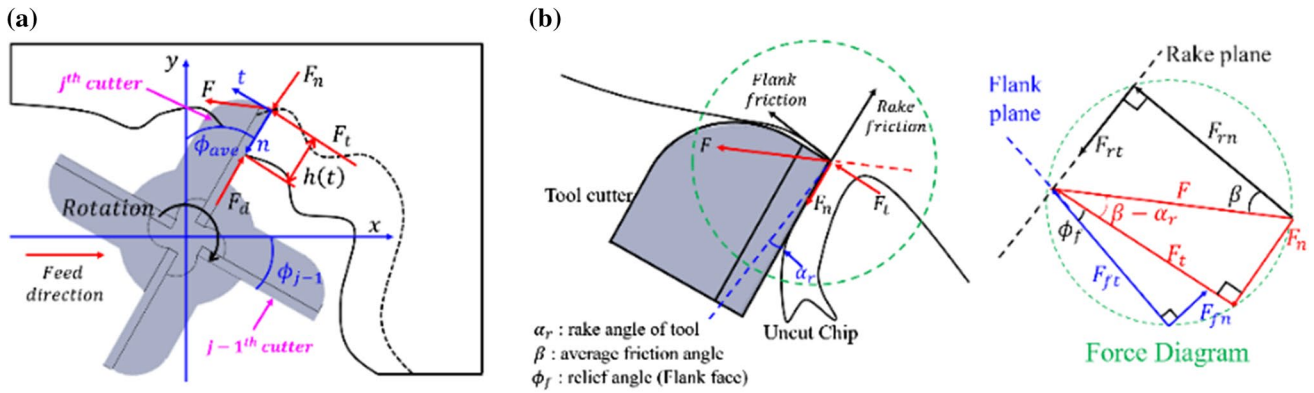
**Fig. 16** 2D model of **a** end milling model and **b** cutting force on tool cutter

dynamic characteristic of spindle system for accurate critical stability prediction. In the actual machining process, thermal conditions vary depending on the environment, therefore it is recommended to use additional experimental conditions or signal processing techniques to find them appropriately.

# Appendix 1: Stability lobe diagram generated by zero-order solution [1]

The stability lobe diagram shows the relationship between the cutting conditions, which is expressed linearly through general equations of the cutting parameters. Partial nonlinear parameters could be applied to the cutting force equation or other terms for solutions, but basically the milling model in Fig. 16 using dynamic chip thickness theory is defined at the first stage, so it starts with the uncut chip thickness calculation.

$$h(\phi_j) = [s_t \sin(\phi_j) + (v_{j,0} - v_j)] g(\phi_j),$$
$$\text{where } g(\phi_j) = 1(\phi_{st} < \phi_j < \phi_{ex}) \text{ or } 0 \,(others) \quad (15)$$

The static chip calculation process could be omitted, since it is not included in the dynamic chip load generation mechanism. When the cutter of the tool cuts the workpiece and comes into contact with the chip, the cutting forces are generated as in Eq. (16):

$$F_{xj} = -F_{tj}\cos(\phi_j) - F_{rj}\sin(\phi_j), F_{yj} = F_{tj}\sin(\phi_j) - F_{rj}\cos(\phi_j)$$
$$\text{where } F_{tj} = K_t a_d h(\phi_j), F_{rj} = K_r F_{tj} \quad (16)$$

Since the cutting forces are exerted on all cutters, those for the milling tool having N cutters are equal to the sum of those force components applied to each cutter, as in Eq. (17):

$$F_x = \sum_{j=0}^{N-1} F_{xj}(\phi_j) \text{ and } F_y = \sum_{j=0}^{N-1} F_{yj}(\phi_j) : \left\{ \begin{array}{c} F_x \\ F_y \end{array} \right\}$$
$$= \frac{1}{2} a_d K_t \begin{bmatrix} \alpha_{xx} & \alpha_{xy} \\ \alpha_{yx} & \alpha_{yy} \end{bmatrix} \left\{ \begin{array}{c} \Delta x \\ \Delta y \end{array} \right\} \quad (17)$$

The angular position of the cutter is changed in accordance with time and the angular velocity, which are transformed into the frequency domain using a Fourier transformation based on the convolution integral. As the definition of the time-varying constants is determined by the cutter of the milling tool rotating at the start-exit angle, it is calculated by the touch point between the radial immersion and workpiece (18).

$$F(t) = \frac{1}{2} a_d K_t [A(t)]\{\Delta t\} \, or \, \{F(\omega)\} = \frac{1}{2} a_d K_t \{[A(\omega)] * (\Delta\omega)\} \quad (18)$$

Fourier coefficients 'A' are approximated if the harmonic number is equal to zero, and the average component of the series expansion is entered into the governing equations. The time period is switched into the angular position of the milling cutters, which shows from the start angle to the exit angle position. If it considers the vibration vector is in the frequency domain, Eqs. (19) and (20) are as follows:

$$F(\omega) = \frac{1}{2} a_d K_t \left\{ \left[ [A_0] \left[ 1 - e^{-i\omega T} \right] [\Phi_0(i\omega)] \{F(\omega)\} \right] \right\} \quad (19)$$

$$[A_0] = \frac{1}{\eta} \int_0^\eta [A(t)]dt = \frac{1}{\phi_p} \int_{\phi_{st}}^{\phi_{ex}} [A(\phi)]d\phi = \frac{N}{2\pi} \begin{bmatrix} \alpha_{xx} & \alpha_{xy} \\ \alpha_{yx} & \alpha_{yy} \end{bmatrix} \quad (20)$$

The directional force coefficients in matrix 'A' are valid for simplifying other geometrical constraints, and the critical

stable conditions of the chatter frequency will be calculated by the characteristic equation from the determinant of F(w). Eigenvalues include solutions for the chatter frequency, static cutting force coefficients, radial immersion angles between cutter and workpiece, and FRF structure (21, 22).

$$
\det \left[ [I] - \frac{1}{2} K_t a_d \left(1 - e^{-i\omega_c \eta}\right) [A_0] \left[\Phi_0\left(i\omega_c\right)\right] \right]
= 0, \; where \; \Lambda = -\frac{N}{4\pi} a_d K_t \left(1 - e^{-i\omega_c \eta}\right) \tag{21}
$$

$$
when \; \Phi_{xy} = \Phi_{yx} = 0 \; : \; a_0 \Lambda^2 + a_1 \Lambda + 1 = 0
$$

$$
where \; a_0 = \Phi_{xx}\left(i\omega_c\right)\Phi_{yy}\left(i\omega_c\right)\left(\alpha_{xx}\alpha_{yy} - \alpha_{xy}\alpha_{yx}\right), \\
and \, a_1 = \alpha_{xx}\Phi_{xx}\left(i\omega_c\right) + \alpha_{yy}\Phi_{yy}\left(i\omega_c\right) \tag{22}
$$

Regardless of the number of vibration modes, a simple quadratic function with two constants has the eigenvalue obtained as below if the system keeps considering the plane of the cut in two degrees of freedom. The eigenvalue consists of a real and imaginary part, where it substitutes exponential terms into a trigonometric function. The critical depth of the cut at the chatter frequency is the same as in Eq. (23).

$$
a_{d,lim} = -\frac{2\pi}{NK_t} \left[ \frac{\Lambda_R\{1 - \cos\left(\omega_c\eta\right)\} + \Lambda_I \sin\left(\omega_c\eta\right)}{1 - \cos\left(\omega_c\eta\right)} \right. \\
\left. +i \frac{\Lambda_I\{1 - \cos\left(\omega_c\eta\right)\} - \Lambda_R \sin\left(\omega_c\eta\right)}{1 - \cos\left(\omega_c\eta\right)} \right] \tag{23}
$$

The depth of cut is a real-value term in the limit of axial depth, and the phase shift of the eigenvalue problem is matched with the spindle speed, where the axial depth of cut counts toward the critical stability of respective cutting conditions. Minimum depth of cut is calculated when chatter frequency is corresponding to each spindle speed values in accordance with constant 'k' in Eqs. 24 and 25

$$
stable \; axial \; depth \; of \; cut \; limit \; : \; a_{d,lim} = -\frac{2\pi\Lambda_R}{NK_t}\left(1 + \kappa^2\right) \tag{24}
$$

$$
corresponding \; spindle \; speed \; : \; n = \frac{60}{N\eta} = \frac{60}{N}\left(\frac{\omega_c}{\epsilon + 2k\pi}\right) \tag{25}
$$

## References

1. Altintas, Y. (2000). *Manufacturing automation: Metal cutting mechanics, machine tool vibrations, and CNC design*. Cambridge University Press.
2. Yue, C., Gao, H., Liu, X., Liang, S. Y., & Wang, L. (2019). A review of chatter vibration research in milling. *Chinese Journal of Aeronautics, 32*(2), 215–242.
3. Bayly, P. V., Mann, B. P., Schmitz, T. L., Peters, D. A., Stépán, G., & Insperger, T. (2002). Effects of radial immersion and cutting direction on chatter instability in end-milling. *ASME International Mechanical Engineering Congress and Exposition, 3461*, 351–363.
4. Insperger, T., Mann, B. P., Stépán, G., & Bayly, P. V. (2003). Stability of up-milling and down-milling, part 1: Alternative analytical methods. *International Journal of Machine Tools and Manufacture, 43*, 25–34.
5. Ertürk, A., Budak, E., & Özgüven, H. N. (2007). Selection of design and operational parameters in spindle–holder–tool assemblies for maximum chatter stability by using a new analytical model. *International Journal of Machine Tools and Manufacture, 47*, 1401–1409.
6. Altintas, Y., Stepan, G., Merdol, D., & Dombovari, Z. (2008). Chatter stability of milling in frequency and discrete time domain. *CIRP Journal of Manufacturing Science and Technology, 1*, 35–44.
7. Özsahin, O., Budak, E., & Özgüven, H. N. (2015). In-process tool point FRF identification under operational conditions using inverse stability solution. *International Journal of Machine Tools and Manufacture, 89*, 64–73.
8. Tong, V., Hwang, J., Shim, J., Oh, J., & Hong, S. (2020). Multi-objective optimization of machine tool spindle-bearing system. *International Journal of Precision Engineering and Manufacturing, 21*, 1885–1902.
9. Yao, Q., Wu, B., Luo, M., & Zhang, D. (2018). On-line cutting force coefficients identification for bull-end milling process with vibration. *Measurement, 125*, 243–253.
10. Tong, V., & Hong, S. (2016). Rolling-element bearing modeling: A review. *International Journal of Precision Engineering and Manufacturing, 17*(12), 1729–1749.
11. Tong, V., & Hong, S. (2018). Improved formulation for running torque in angular contact ball bearings. *International Journal of Precision Engineering and Manufacturing, 19*(1), 47–56.
12. Xiong, G. L., Yi, J. M., Zeng, C., Guo, H. K., & Li, L. X. (2003). Study of the gyroscopic effect of the spindle on the stability characteristics of the milling system. *Journal of Materials Processing Technology, 138*, 379–384.
13. Movahhedy, M. R., & Mosaddegh, P. (2006). Prediction of chatter in high speed milling including gyroscopic effects. *International Journal of Machine Tools and Manufacture, 46*, 996–1001.
14. Gagnol, V., Bouzgarrou, B. C., Ray, P., & Barra, C. (2007). Model-based chatter stability prediction for high-speed spindles. *International Journal of Machine Tools and Manufacture, 47*(7–8), 1176–1186.
15. Xu, X., Tang, W., & Sun, S. (2010). Research of gyroscopic effects on the stability of high speed milling. *Key Engineering Materials, 431–432*, 369–372.
16. Cao, H., Li, B., & He, Z. (2012). Chatter stability of milling with speed-varying dynamics of spindles. *International Journal of Machine Tools and Manufacture, 52*, 50–58.
17. Tajalli, S. A., Movahhedy, M. R., & Akbari, J. (2012). Investigation of the effects of process damping on chatter instability in micro end milling. *Proceedings of CIRP, 1*, 156–161.
18. Shi, Y., Mahr, F., Wagner, U. V., & Uhlmann, E. (2013). Gyroscopic and mode interaction effects on micro-end mill dynamics

and chatter stability. *The International Journal of Advanced Manufacturing Technology, 65*, 895–907.

19. Grossi, N., Scippa, A., Sallese, L., Sato, R., & Campatelli, G. (2015). Spindle speed ramp-up test: A novel experimental approach for chatter stability detection. *International Journal of Machine Tools and Manufacture, 89*, 221–230.

20. Özşahin, O., Budak, E., & Özgüven, H. N. (2015). Identification of bearing dynamics under operational conditions for chatter stability prediction in high speed machining. *Precision Engineering, 42*, 53–65.

21. Wang, J. J., Uhlmann, E., Oberschmidt, D., Sung, C. F., & Perfilov, I. (2016). Critical depth of cut and asymptotic spindle speed for chatter in micro milling with process damping. *CIRP Annals-Manufacturing Technology, 65*(1), 113–116.

22. Lu, X., Jia, Z., Liu, S., Yang, K., Feng, Y., & Liang, S. Y. (2019). Chatter stability of micro-milling by considering the centrifugal force and gyroscopic effect of the spindle. *Journal of Manufacturing Science and Engineering, 141*(11), 111003. https://doi.org/10.1115/1.4044520

23. Chen, J. S., & Hsu, W. Y. (2003). Characterizations and models for the thermal growth of a motorized high-speed spindle. *International Journal of Machine Tools and Manufacture, 43*(11), 1163–1170.

24. Li, H. Q., & Shin, Y. C. (2004). Analysis of bearing configuration effects on high speed spindles using an integrated dynamic thermos-mechanical spindle model. *International Journal of Machine Tools and Manufacture, 44*, 347–364.

25. Kim, S.-M., Lee, S.-K., & Lee, K. J. (2002). Effect of bearing surroundings on the high-speed spindle-bearing compliance. *International Journal of Advanced Manufacturing Technology, 19*(8), 551–557.

26. Holkup, T., Cao, H., Kolar, P., Altintas, Y., & Zeleny, J. (2010). Thermo-mechanical model of spindles. *CIRP Annals, 59*(1), 365–368.

27. Jin, X., & Altintas, Y. (2013). Chatter stability model of micromilling with process damping. *Journal of Manufacturing Science and Engineering, 135*(3), 031011.

28. Graham, E., Mehrpouya, M., & Park, S. (2013). Robust prediction of chatter stability in milling based on the analytical chatter stability. *Journal of Manufacturing Processes, 15*, 508–517.

29. Hajmohammadi, M. S., Movahhedy, M. R., & Moradi, H. (2014). Investigation of thermal effects on machining chatter based on FEM simulation of chip formation. *CIRP Journal of Manufacturing Science and Technology, 7*(1), 1–10.

30. Ma, C., Mei, X., Yang, J., Zhao, L., & Shi, H. (2015). Thermal characteristics analysis and experimental study on the high-speed spindle system. *The International Journal of Advanced Manufacturing Technology, 79*(1–4), 469–489.

31. Liu, T., Gao, W. G., Zhang, D. W., Zhang, Y. F., Chang, W. F., Liang, C. M., & Tian, Y. L. (2017). Analytical modeling for thermal errors of motorized spindle unit. *International Journal of Machine Tools and Manufacture, 112*(1), 53–70.

32. Grossi, N., Montevecchi, F., & Sallese, L. (2017). Chatter stability prediction for high-speed milling through a novel experimental-analytical approach. *International Journal of Advanced Manufacturing Technology, 89*(9–12), 2587–2601.

33. Qu, S., Zhao, J., & Wang, T. (2017). Experimental study and machining parameter optimization in milling thin-walled plates based on NSGA-II. *International Journal of Advanced Manufacturing Technology, 89*(5–8), 2399–2409.

34. Wang, C., Zhang, X., Liu, Y., Cao, H., & Chen, X. (2018). Stiffness variation method for milling chatter suppression via piezoelectric stack actuators. *International Journal of Machine Tools and Manufacture, 124*, 53–66.

35. Liu, J. F., Lai, T., & Tie, G. P. (2018). Influence of thermo-mechanical coupled behaviors on milling stability of high speed motorized spindles. *Precision Engineering, 52*, 94–105.

36. Li, D., Cao, H., Liu, J., Zhang, X., & Chen, X. (2019). Milling chatter control based on asymmetric stiffness. *International Journal of Machine Tools and Manufacture, 147*, 103458.

37. Wan, S., Jin, X., Maroju, N. K., & Hong, J. (2019). Effect of vibration assistance on chatter stability in milling. *International Journal of Machine Tools and Manufacture, 145*, 103432.

38. Wu, G., Li, G., Pan, W., Wang, X., & Ding, S. (2020). A prediction model for the milling of thin-wall parts considering thermal-mechanical coupling and tool wear. *International Journal of Advanced Manufacturing Technology, 107*, 4645–4659.

39. Postel, M., Özşahin, O., & Altintas, Y. (2018). High speed tooltip FRF predictions of arbitrary tool-holder combinations based on operational spindle identification. *International Journal of Machine Tools and Manufacture, 129*, 48–60.

40. Quintana, G., Ciurana, J., & Teixidor, D. (2008). A new experimental methodology for identification of stability lobes diagram in milling operations. *International Journal of Machine Tools and Manufacture, 48*(15), 1637–1645.

41. Kakinuma, Y., Sudo, Y., & Aoyama, T. (2011). Detection of chatter vibration in end milling applying disturbance observer. *CIRP Annals-Manufacturing Technology, 60*, 109–112.

42. Wan, C. (2005). *Analysis of rolling element bearings* (p. 2005). Wiley.

43. Harris, T. A., & Kotzalas, M. N. (2006). *Rolling bearing analysis* (5th ed.). Taylor & Francis.

44. Hartnett, M. (1979). Analysis of contact stresses in rolling element bearings. *Journal of Lubrication Technology, 101*(1), 105–109.

**Minsu Kim** Ph.D candidate of Gwangju Institute of Science and Technology from 2017, Master degree in Mechanical Engineering at Gwangju Institute of Science and Technology in 2017. Research area : metal cutting mechanics including chatter vibration theory, ultraprecision machining., and CFRP machining.

**Hyung-Wook Park** Professor of Ulsan National Institute of Science and Technology from 2009, PhD in Mechanical Engineering at Georgia Institute of Technology, USA in 2008. Research area : Micro/Macro machining, machining dynamics, robot arm machining, and Multi-Physics based Micro/Meso-scale Manufacturing (MP-M2) Processes and Systems.

**Sun-Kyu Lee** Professor of Gwangju Institute of Science and Technology from 1994, PhD in Mechanical Engineering for Production at Tokyo Institute of Technology in 1991. Research area : Ultraprecision machine systems, Precision measurement, Thermo-mechanical design.